

Effects of He-ion irradiation on the microstructures and mechanical properties of the novel Co-free $V_xCrFeMnNi_y$ high-entropy alloys



Huanzhi Zhang^a, Chunhui Li^a, Zhenbo Zhu^b, Hefei Huang^{b,*}, Yiping Lu^{a,*}, Tongmin Wang^a, Tinigju Li^a

^a Key Laboratory of Solidification Control and Digital Preparation Technology, School of Materials Science and Engineering, Dalian University of Technology, Dalian, Liaoning 116024, China

^b Shanghai Institute of Applied Physics, Chinese Academy of Sciences (CAS), Shanghai 201800, China

ARTICLE INFO

Article history:

Received 26 June 2022

Revised 5 October 2022

Accepted 6 October 2022

Available online 7 October 2022

Keywords:

High-entropy alloys

Helium bubbles

Microstructures

Irradiation tolerance

Mechanical properties

ABSTRACT

High-entropy alloys (HEAs), as a promising candidate structural material for advanced nuclear energy system, have been widely studied recently due to the combination of the outstanding irradiation tolerance and enhanced mechanical properties at elevated temperatures. In this study, an FCC-structured CrFeMnNi₂ HEA and a BCC-structured VCrFeMn HEA without Co element were designed and prepared. The effects of He-ion irradiation on the microstructures and mechanical properties were investigated, so as to preliminarily evaluate the irradiation tolerance of the novel Co-free HEAs. At fluences of 3×10^{16} and 6×10^{16} ions/cm², the CrFeMnNi₂ and VCrFeMn HEAs showed good structural stability at 1023 K; the transmission electron microscope results revealed no amorphization/precipitations. The average sizes and number densities of He bubbles increased as the fluence improved for the two alloys. At each fluence, the average size of the He bubbles in the VCrFeMn HEA was larger than that in the CrFeMnNi₂ HEA, while the number density and volume fraction were lower. The CrFeMnNi₂ HEA possessed a higher hardening fraction (77%), and an irradiation-induced hardening saturation was observed in the VCrFeMn HEA with a lower hardening fraction of 33%. The experimental results indicated that the novel low-activation VCr-FeMn HEA might be a competitive candidate structural material for advanced reactors. The mechanisms of the irradiation tolerance of Co-free HEAs were also discussed.

© 2022 Elsevier B.V. All rights reserved.

1. Introduction

As one of the decisive factors for the safe and efficient operation of nuclear reactors, structural materials have been identified as an important component in developing nuclear power [1–3]. The stringent working environment in the next-generation fission/future fusion nuclear reactors poses a major challenge to the design of structural materials [4,5]. After 316 austenitic stainless steel, the emerging materials for structural components (such as reduced activation ferritic/martensitic [6,7], oxide dispersion-strengthened steels [8,9], V-based alloys [10,11] and SiC/SiC composites [12,13]) have been developed rapidly, and some positive results have been obtained. Among the emerging materials, high-entropy alloys (HEAs) [14–16] have shown outstanding competitiveness owing to their unique structures and properties. The combination of enhanced material properties, such as excellent stabil-

ity at elevated temperatures [17,18], high strength [19,20], good corrosion resistance [21,22], and impressive irradiation tolerance [1,5,23–25], promotes the application potential of HEAs under extreme conditions, which qualifies the HEAs as a promising candidate structure material for the advanced nuclear energy system. Recently, the ion irradiation experiments with high fluences were performed at room and elevated temperatures. The results manifested that certain HEAs [1,26,27] with special chemical constituents exhibited much better irradiation performance than conventional alloys for the particular self-healing characteristic. The severe lattice distortion and sluggish diffusion caused by atomic size difference, as well as the chemical complexity, contributed to the inhibited dislocation loop growth [28,29], low void swelling [5,30], and suppressed irradiation-induced segregation [31,32] of HEAs under ion irradiation. Specifically, two hypotheses about the effective means of point defect recombination were proposed for HEAs: first, the increase in chemical complexity (especially for the number of principal elements) reduces the electron mean free path and thermal conductivity and thus favors a longer thermal spike and slower energy dissipation, which could affect the dynamics of

* Corresponding authors.

E-mail addresses: huanghefei@sinap.ac.cn (H. Huang), luyiping@dlut.edu.cn (Y. Lu).

defects and lead to a reduction in residual defects [33]. Second, the enhanced overlap of interstitial and vacancy migration energy distributions for HEAs would promote the thermal point defect recombination [2,25].

The alloys containing 3d-transition elements (such as Co, Cr, Fe, Mn, and Ni elements) are the main research objects of the irradiation damage studies of HEAs at present, while the application of Co-contained alloys is restricted in nuclear industry [34,35]. The materials with high-activation elements (such as Co, Nb, and Mo elements) endanger the environment and safety of workers by producing high-level radioactive waste after neutron irradiation in the core reactors [36,37]. As a result, low activation is considered to be an indispensable design standard for structural materials in advanced reactors [25,34,38,39]. In addition, recent studies on the irradiation performance of HEAs mainly focus on the impact of the number, types, and atomic percentage of alloying elements, while the study on the influence of structure is quite limited [30]. Hence, in this study, the Co-free $V_xCrFeMnNi_y$ HEAs were designed to explore the effects of ion fluence and structure on the irradiation performance. All the selected five elements have relatively low thermal neutron absorption cross-section, which makes the alloys suitable for accident tolerant fuel (ATF) claddings materials [27]. Moreover, the VCrFeMn alloy is a newly developed low-activation HEA [34,37,40], which meets the material design concept of the next-generation nuclear energy system. The V element is beneficial to the yield strength improvement of the alloys and facilitates the formation of the body-centered cubic (BCC) structure; the Cr element has good corrosion resistance; the Fe and Mn elements possess good comprehensive performance; and the Ni element exhibits fine ductility. Therefore, novel Co-free $V_xCrFeMnNi_y$ HEAs were prepared by vacuum-arc melting, and the microstructures, mechanical properties, and irradiation tolerance of the $V_xCrFeMnNi_y$ HEAs were studied in detail.

2. Experimental process

2.1. Material preparation

In this study, raw materials with the purities of more than 99.9 wt% were selected to manufacture the $V_xCrFeMnNi_y$ alloys. Under the high-purity argon atmosphere, the $V_xCrFeMnNi_y$ ($x = 0, y = 2$; $x = 1, y = 0$; the alloys were denoted as V0 and V1, respectively) alloys were prepared by arc melting in a water-cooled copper crucible. The alloys were remelted for more than seven times to ensure the uniform distribution of the elements. For the pristine and irradiated samples, the crystal structures were identified by x-ray diffraction (XRD; Empyrean with Kα1 radiation source) operated at 30 kV and 20 mA, with the 2θ ranging from 20° to 100°. The microstructures and elemental distribution of the specimens were identified using a JXA-8530F PLUS electron probe micro analysis (EPMA) equipped with a wavelength-dispersive spectrometry (WDS). A DNS-100 uniaxial compression tester was introduced to determine the mechanical properties of the as-cast alloys with cylindrical specimens of sizes of $\Phi 5 \times 10$ mm at a strain rate of $1 \times 10^{-3}/s$.

2.2. Ion irradiation

Around the melting point temperature (T_m), the influence of He bubble formation on the decline of the mechanical properties of structural materials in advanced reactors has always been a concern [41]. Therefore, the irradiation performance of the $V_xCrFeMnNi_y$ alloys was studied by He ion beam irradiation at 1023 K (0.57 T_m and 0.53 T_m for V0 and V1 alloys, respectively). The specimens with a dimension of $1 \times 6.5 \times 10$ mm for the irradiation experiment were cut from the as-cast ingots and then sub-

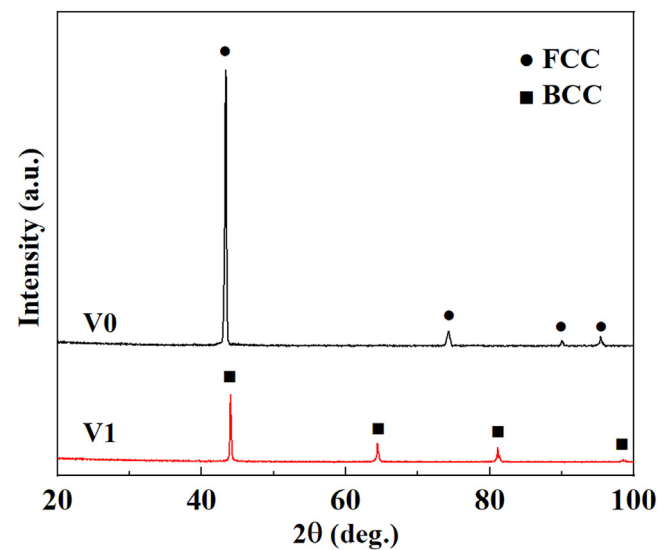


Fig. 1. XRD patterns of the as-cast $V_xCrFeMnNi_y$ alloys.

jected to mechanical polishing and electropolishing to optimize the surface. The prepared specimens were irradiated with 1 MeV He ions at fluences of 3×10^{16} and 6×10^{16} ions/cm², using a 4-MV Pelletron accelerator located at the Shanghai Institute of Applied Physics, Chinese Academy of Sciences. The Stopping and Range of Ions in Materials 2008 (SRIM 2008) software was employed to calculate the depth damage profile of the V0 and V1 alloys in this study, as shown in Fig. 5a and 5b. The displacement energy for each involved element (V, Fe, Cr, Mn, and Ni) was set as 40 eV [42,43]. At the fluence of 6×10^{16} ions/cm², the peak He concentrations and displacement doses caused by He-ion irradiation were ~2.9 at%, 1.3 displacements per atom (dpa) and 3.3 at%, 1.3 dpa for the V0 and V1 alloys, respectively. For both alloys, the peak positions of the displacement appeared at a depth of ~1600 nm, and the maximum damage depth was ~1900 nm according to the simulation results of SRIM 2008. The transmission electron microscope (TEM) was used to study the microstructures of the irradiated samples. Cross-sectional TEM samples were cut from the ion irradiation surface by the focused ion beam (FIB) of a FEI Helios G4 UX instrument, and the thickness of the samples was about 60 nm. For investigating the irradiation effect on mechanical properties, the G200 nanoindenter was introduced to determine the hardness of the pristine and irradiated samples. More than eight indents were prepared on the irradiated surface for each sample to minimize the measurement error.

3. Results and discussion

3.1. Microstructures of as-cast $V_xCrFeMnNi_y$ alloys

The XRD patterns of the as-cast samples of $V_xCrFeMnNi_y$ alloys are shown in Fig. 1, in which the diffraction peaks of two cubic structures are presented. The V0 alloy displayed a single face-centered cubic (FCC) solid solution structure, and the V1 alloy showed a BCC solid solution structure, which implies the change in the crystal structure with the addition of V element.

The microstructures of the $V_xCrFeMnNi_y$ alloys are presented in Fig. 2. Both the V0 and V1 alloys showed a single-phase structure. Combined with the XRD results, the single-phase structure in the V0 alloy was confirmed as the FCC solid solution, while the V1 alloy consisted of a single-phase BCC structure, suggesting that the V element was conducive to the formation of the BCC structure.

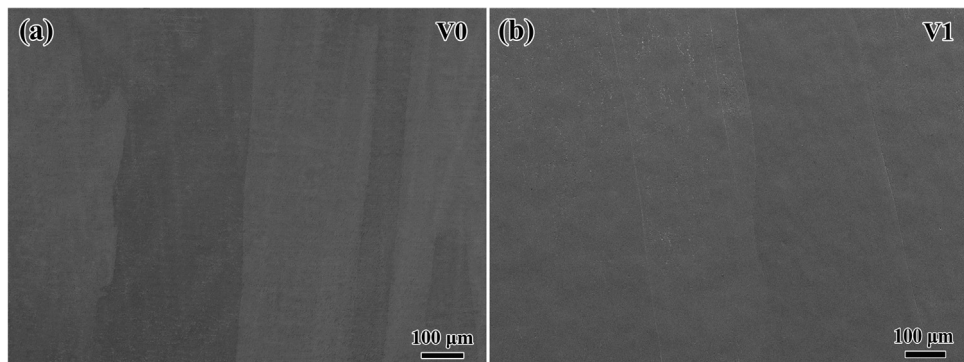


Fig. 2. Back-scattered electron images of the microstructures of $V_xCrFeMnNi_y$ alloys: (a) V0 alloy and (b) V1 alloy.

Table 1
Empirical parameters of $V_xCrFeMnNi_y$ HEAs.

Alloy	Phase	S_{mix} (J/(K mol))	ΔH_{mix} (kJ/mol)	δ (%)	VEC	Ω
V0	FCC	11.08	-5.28	3.31	8.20	3.76
V1	BCC	11.53	-2.25	3.55	6.50	9.85

Table 2
Yield strength and plastic strain of $V_xCrFeMnNi_y$ ($x = 0, y = 2$; $x = 1, y = 0$; the alloys were denoted as V0 and V1, respectively) alloys.

Alloy	Yield strength (MPa)	Plastic strain (%)
V0	113	>50
V1	660	>50

Frequently used empirical parameters for the phase formation rules of HEAs included valence electron concentration (VEC), atomic size difference (δ), solid solution formability (Ω), configurational entropy (ΔS_{mix}), and enthalpy of mixing (ΔH_{mix}). The details of the definitions and calculation formulas of the involved empirical parameters could be acquired from previous studies [44–46]. Guo et al. [44] proposed that BCC phase usually forms when the value of VEC is less than 6.87, and FCC phase is found at VEC > 8. Additionally, Yang and Zhang [46] concluded that the conditions of $\Omega > 1.1$ and $\delta < 6.6\%$ are necessary for the formation of simple solid-solution phase in most HEAs. The empirical parameters for the $V_xCrFeMnNi_y$ alloys are summarized in Table 1. For the two alloys, the maximal δ was 3.55% (< 6.6%), the minimum Ω was 3.76 (> 1.1), and the values of ΔH_{mix} were in the region from -15 to 5 kJ/mol. All the calculated empirical parameters and the high ΔS_{mix} (11.08 J/(K mol)) could predict the formation of the solid-solution phase, which was consistent with the experimental results. The values of VEC for the V0 and V1 alloys were 8.20, and 6.50, respectively, corresponding to the FCC and BCC structures, which verified the applicability of the theory proposed by Guo et al. [44].

3.2. . Mechanical properties of the as-cast $V_xCrFeMnNi_y$ alloys

The compressive stress-strain curves of the $V_xCrFeMnNi_y$ alloys measured at room temperature are plotted in Fig. 3. Specific values of the yield strength and plastic strain are summarized in Table 2. The mechanical behaviors of the $V_xCrFeMnNi_y$ alloys were obviously affected by the addition of V element. The yield strength of the FCC-structured V0 alloy was lower, while that of the BCC-structured V1 alloy was high due to the formation of the hard BCC phase. Simultaneously, the addition of V element could hardly cause a significant reduction in the plasticity of the V1 alloy. As shown in Table 2, the $V_xCrFeMnNi_y$ HEAs showed a plastic strain of more than 50% without fracture during compression.

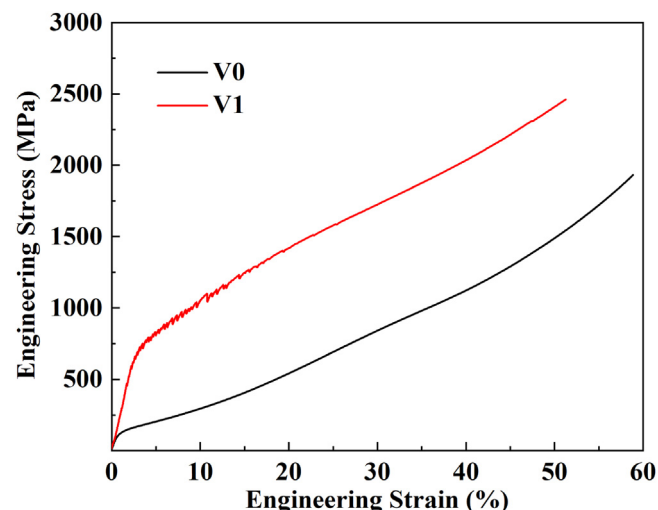


Fig. 3. Compressive stress-strain curves of $V_xCrMnFeNi_y$ alloys.

The novel Co-free $V_xCrFeMnNi_y$ HEAs possessed good comprehensive mechanical properties, which was beneficial to the industrial application prospects, especially for the low-activation V1 HEA with a yield strength of 660 MPa. Furthermore, the irradiation performance of the Co-free HEAs was studied using the He-ion irradiation experiment to preliminarily explore the possibility of the novel alloys as candidate structural materials of the advanced nuclear energy system.

3.3. . XRD analysis of the irradiated alloys

As shown in Fig. 4, the effects of He-ion irradiation on the V0 and V1 alloys were studied using XRD tests. After irradiation to the fluences of 3×10^{16} and 6×10^{16} ions/cm² at 1023 K, only diffraction peaks for the FCC and BCC solid solution phases emerged in the V0 and V1 alloys, respectively, which was consistent with the as-cast alloys. Therefore, the designed V0 and V1 alloys showed structural stability under the given irradiation condition.

As exhibited in Fig. 4b, almost no (111) peak shift was observed in XRD patterns of the irradiated V0 alloy compared with that of the pristine one, which implied that the lattice constants did not change obviously after He-ion irradiation. This also proved the stable crystal structure of the V0 alloy under He-ion irradiation. Similar findings were detected in the reported HEAs [27]. As the irradiation dose improved, the (110) peaks for V1 alloy shifted slightly to lower 2θ after irradiation with the corresponding lattice constant increasing from 0.2895 to 0.2904 nm, and the rate of change was no more than 0.31% at both irradiation fluences. The high-

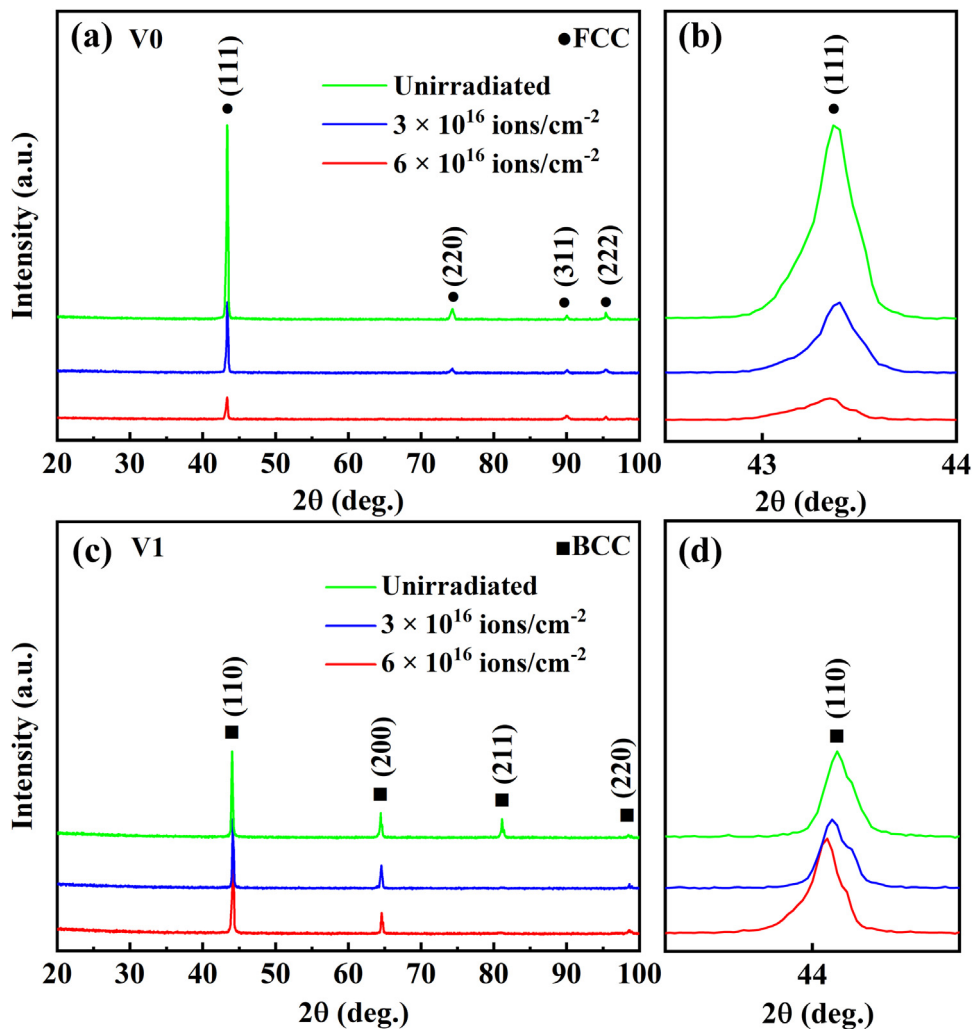


Fig. 4. XRD patterns of the unirradiated and irradiated (a) V0 and (c) V1 alloys at different fluences; detailed scans of (b) (111) peaks and (d) (110) peaks.

temperature condition tended to release the residual stress, eliminate the defects, and lighten the lattice distortion, which favored the decrease in the lattice constant. However, the defects (point defects and their clusters, dislocation loops) and micro-strain in the lattice structure caused by ion irradiation could promote the lattice expansion of irradiated alloys, contributing to the variation in the XRD patterns of the V1 alloy. The results of lattice expansion of the V1 alloy after irradiation were consistent with those of traditional alloys [8,47,48] and some HEAs [49,50], but opposite to the findings obtained by Lu et al. [1], who showed an abnormal decline of lattice constant in the Ti₂ZrHfV_{0.5}Mo_{0.2} HEA after He-ion irradiation. The change in lattice constant for HEAs after irradiation at elevated temperatures is worth studying further.

3.4. TEM characterization

The distribution range, size, shape, and number density specified as the characteristics of He bubbles in the V0 and V1 alloys were investigated. Fig. 5a and 5b shows the comparison between the profiles of SRIM prediction results (the distribution of displacement and implanted He ions with depth) and the overview of microstructures from the surface to a depth of 2500 nm of the irradiated V0 and V1 alloys, respectively. The TEM bright field (BF) images indicated that the damaged bands showing dark contrast appeared at a depth of ~1600 nm and extended to ~1900 nm for

the two alloys. Specifically, the He bubbles formed along the direction of the irradiation depth and the positions of the bubble peak region were consistent with the SRIM simulation results.

For a clear comparison of the He bubble distribution in the V0 and V1 alloys at different fluences, the TEM images photographed at the same depth range (from ~1500 to 2000 nm) were selected, as shown in Fig. 5c–f, sharing the same scale bar. The images in Fig. 5c–f roughly exhibit the peak damage region in which the vast majority of the He bubbles were distributed. The damage regions of the V0 and V1 alloys appeared at similar positions, which coincided with the simulation results. At different fluences, the positions of peak damage regions (ranging from the depth of ~1600 to 1900 nm) remained almost unchanged for both alloys.

The features of irradiated samples were demonstrated by the under-focused, on-focused, and over-focused TEM-BF images obtained in the same position of the peak damage regions in the V0 and V1 alloys, respectively. As shown in Fig. 6, white and black features of He bubbles were found under different focusing states, and no precipitates were observed. It is possible that precipitates cannot be detected under the conditions where He bubbles were observed. Then the selected area electron diffraction (SAED) was conducted on the irradiated V0 and V1 samples, and the results showed that only the FCC and BCC phase diffraction spots of V0 and V1 alloys can be detected in the SAED patterns obtained from different irradiation damage regions. Therefore, the V0 and V1 al-

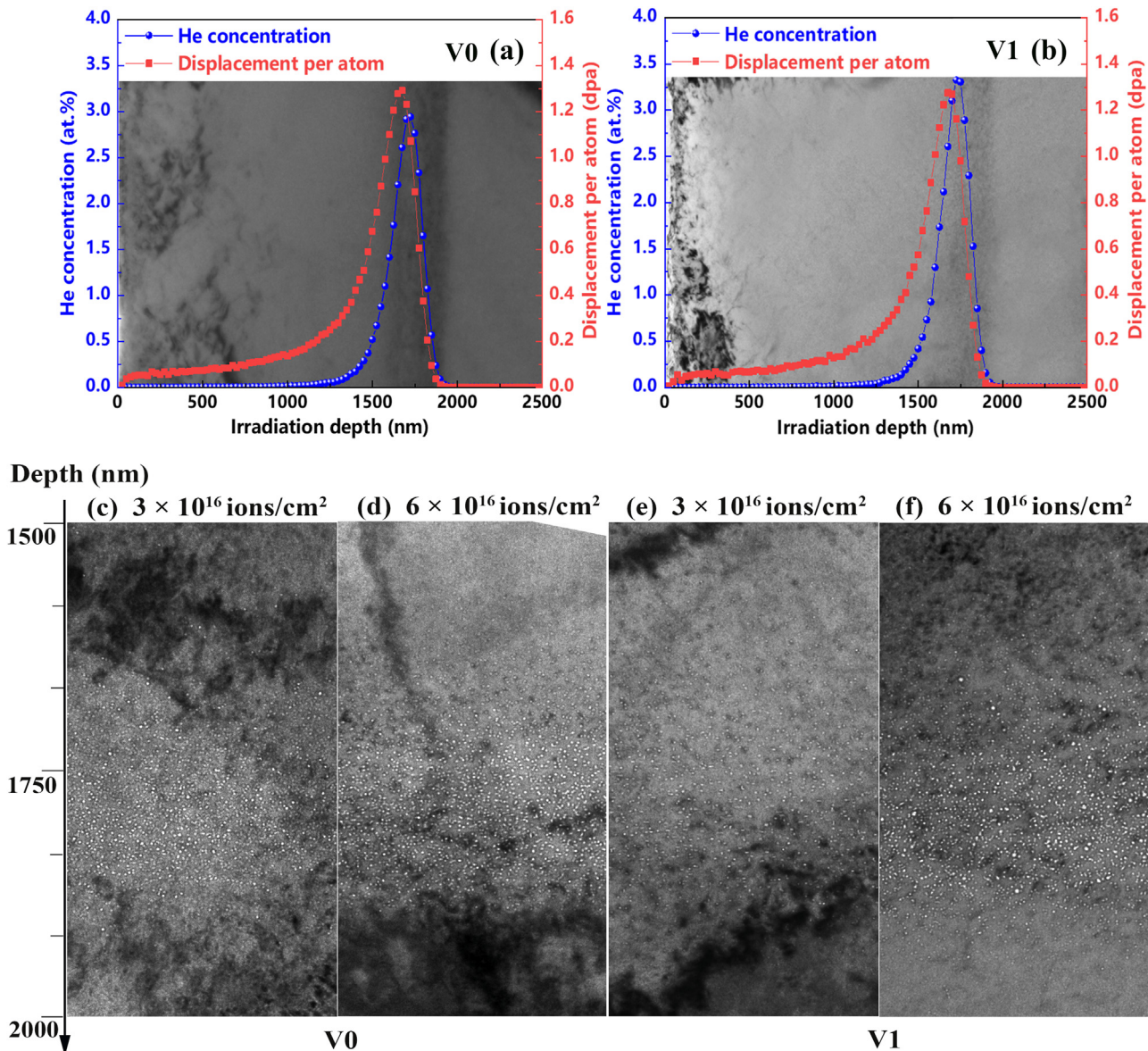


Fig. 5. Profiles of SRIM prediction of the displacement and implanted He ions of (a) V0 and (b) V1 alloys, overlapping with the overview of microstructures from the surface to a depth of 2500 nm; (c-f) a series of cross-sectional TEM images showing the distribution of He bubbles along the depth direction in the V0 and V1 alloys at different fluences.

loys exhibited high stabilities in structure after He ion irradiation.

The He bubble characterizations in the peak damage regions of V0 and V1 alloys irradiated to the two fluences of 3×10^{16} and 6×10^{16} ions/cm² are presented in Fig. 7. The He bubbles showed a uniform and random spatial distribution in all the images, and the bubble sizes presented normal-like distributions (shown in Fig. 8), implying that the nucleation of the He bubbles was a homogeneous process. The single-phase structured V0 and V1 alloys could provide a uniform microstructure for He bubble nucleation.

The spherical He bubbles were detected in the V0 alloy at both fluences, while the faceted bubbles were formed in the V1 alloy at low fluence, which was consistent with the previous findings on BCC-structured HEAs [51]. As the fluence increased, the shape of the He bubbles in V1 alloy changed from faceted to spherical. Besides the state of bubbles, the morphology of He bubbles was mainly controlled by the mechanical and energy characteristics of the solid lattice [52,53]. Generally, the gas pressure in spherical He

bubbles is high, while the one in faceted He bubbles is suppressed. With the increase in irradiation fluence, more implanted He atoms were absorbed by the faceted He bubbles, improving the internal pressure and changing the shape of the bubbles in the V1 alloy. The size distribution (shown in Fig. 8a and 8b) and the number density of He bubbles were investigated using the TEM images acquired from peak damage regions of all the irradiated samples. For the V0 and V1 alloys at each fluence, a tendency of unimodal distribution of the He bubble sizes was observed. The average size (d) and the number density (N) of the He bubbles in the peak damage regions of the V0 and V1 alloys at different fluences are summarized in Table 3. The corresponding histogram is shown in Fig. 8c to intuitively compare the number densities at different fluences. The number densities of He bubbles in both alloys increased as the fluence improved, and the number density of He bubbles in the V0 alloy was larger than that in the V1 alloy at each fluence. The average sizes increased from 2.3 ± 0.6 to 3.4 ± 1.0 nm for the V0 alloy, and from 2.8 ± 0.9 to 3.6 ± 1.1 nm for the V1 alloy, with

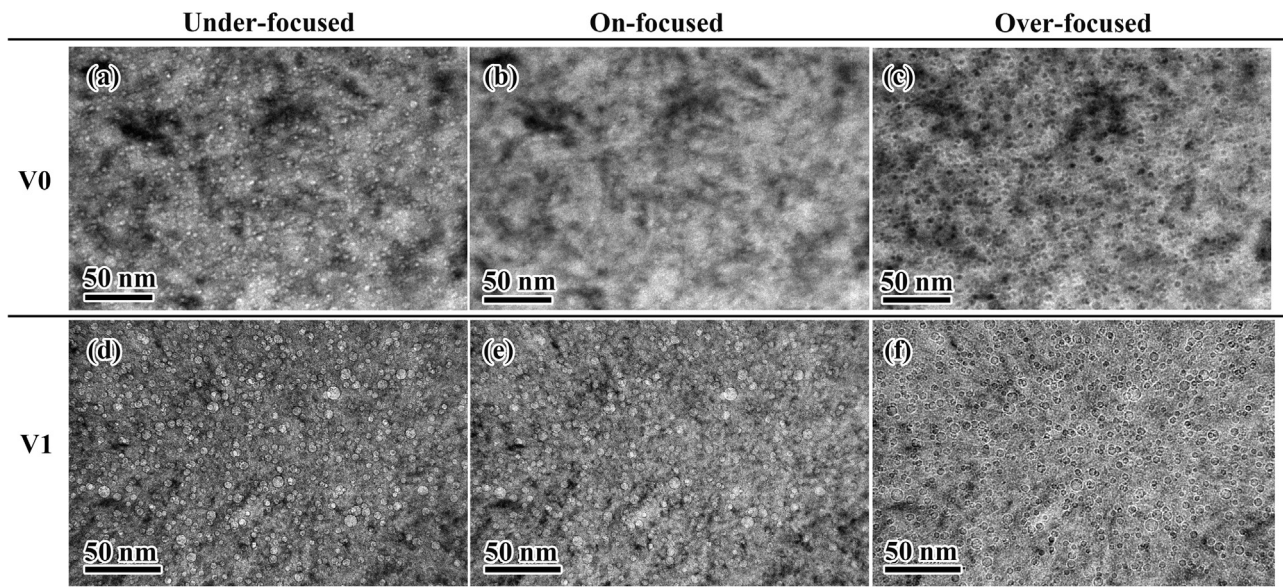


Fig. 6. The under-focused, on-focused, and over-focused images of He bubble characterization acquired in the peak damage regions of the V0 and V1 alloys at the fluence of 6×10^{16} ion/cm².

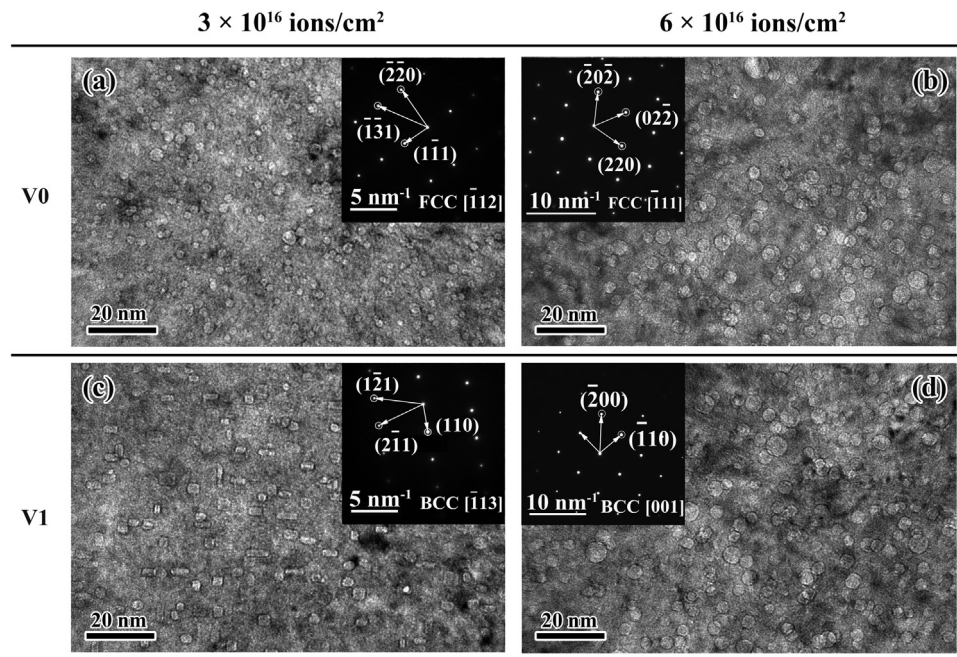


Fig. 7. Comparison of He bubble characterizations in the peak damage regions of the V0 and V1 alloys at different fluences.

Table 3
Average sizes and number densities of He bubbles in the V0 and V1 alloys at different fluences.

Alloy	Average size (nm)		Density ($\times 10^{23}/\text{m}^3$)	
	3×10^{16} ions/cm ²	6×10^{16} ions/cm ²	3×10^{16} ions/cm ²	6×10^{16} ions/cm ²
V0	2.3 ± 0.6	3.4 ± 1.0	3.17	3.44
V1	2.8 ± 0.9	3.6 ± 1.1	1.47	2.81

an improvement in fluence. The statistical results suggested that the average size of He bubbles in the V0 alloy was smaller than that in the V1 alloy at same fluences.

Compared with conventional FCC-structured materials under similar fluence, the average sizes of He bubbles in the V0 alloy are smaller while the densities are larger than those in pure Ni

[41] and Ni-1 wt.% SiC_{NP} alloy [54] (the Ni-1 wt.% SiC_{NP} and V-4Cr-4Ti alloys were denoted as Ni_{SiC} and V_{CrTi} in Table 4). However, the values show the opposite trend to those in GH3535 [55] and 316 L stainless steel [56], as shown in Table 4. For the V1 alloy, the average sizes and densities of He bubbles are comparable to the values of the well-researched BCC-structured alloys (V-4Cr-4Ti

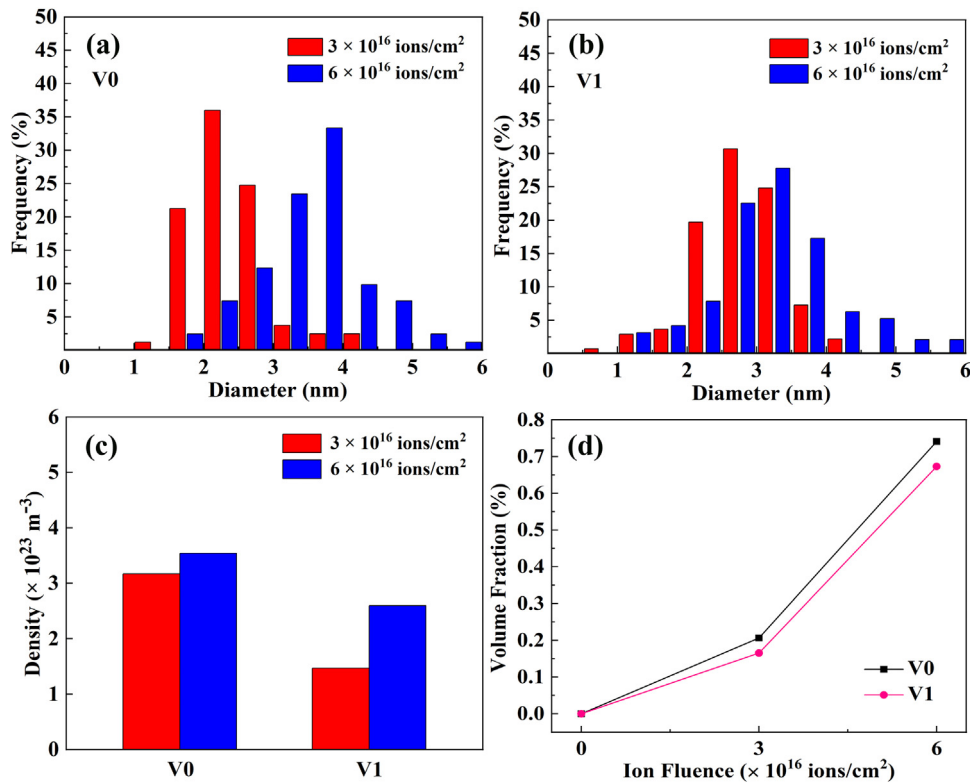


Fig. 8. Distribution of the He bubble size in the He peak regions of the (a) V0 and (b) V1 alloys at different fluences; (c) corresponding He bubble number density; and (d) volume fraction.

Table 4

The average size, number density of He bubbles and hardening fraction of the He-irradiated conventional materials with different structures.

BCC	BCC				FCC			
	CLAM	RAFM	ODS	V_{crit}	316L	NiSiC	GH3535	Ni
Temperature(K)	273	773	723	573	973	923	923	973
Fluence (x 10 ¹⁶ ions/cm ²)	7	3	10	5	10	6	10	1.5
Average size (nm)	5.8	~5.1	3.9	2.7	2.2	8.1	2.3	6.1
Density (x 10 ²³ /m ³)	0.1	–	3.6	3.3	7.1	0.1	9.1	0.3
Hardening fraction (%)	224	86	75	52	75	47	40	–

alloys [57], oxide dispersion-strengthened steels [8], reduced activation ferritic/martensitic steels [58], China low activation martensitic steel [59]). Generally, the growth of He bubbles is temperature sensitive and larger He bubbles were found at elevated temperature [60]. The irradiation experiment temperature of conventional materials (Listed in Table 4) is no more than 973 K, which is lower than that of the V0 and V1 alloys in this study. Even at 1023 K, the average sizes of He bubbles in the V0 and V1 are not larger than 3.3 nm, showing the resistance to He bubble growth. The increasing chemical complexity and enhanced recombination of point defects during irradiation of HEAs are favorable for the formation of small He bubbles [60].

The injected He atoms will diffuse and combine with vacancies to form bubbles due to the limited solubility of He in the metals. The diffusivities and concentrations of He (He atom and He-vacancy complex) and point defects (vacancies and interstitials) determine the growth behavior of He bubbles [60]. The defect concentration in the BCC-structured HEAs could be suppressed for the enhanced recombination of vacancies and interstitials [25]. Hence, the diffusivity of He and/or point defects in the BCC-structured V1 alloy may be higher than that of the V0 alloy, which leads to the larger size and lower number density of He bubbles in the V1 alloy.

The irradiation-induced void swelling produced by the emergence of numerous He bubbles was evaluated by defining the volume fraction (S), which can be described as follows [42]:

$$S = \frac{V_1}{V_2} = \frac{4}{3}\pi r^3 N \quad (1)$$

where V_1 and r represent the total volume and equivalent radius of He bubbles, respectively, and V_2 is the volume of the sample. Only the large He bubbles detected by TEM were considered in this method of estimating void swelling, and the influence of invisible small He bubbles was ignored. The changes in the volume fraction of the V0 and V1 alloys irradiated to the fluences of 3×10^{16} and 6×10^{16} ions/cm² are shown in Fig. 8d. As detected, the volume fraction increased gradually with the increase in fluence for both alloys. At the same fluence, the BCC-structured V1 alloy possessed lower values of volume fraction than the FCC-structured V0 alloy, suggesting better swelling resistance in the V1 alloy.

3.5. Irradiation-induced hardening

The nanoindentation hardness test was employed to investigate the effects of He-ion irradiation on the mechanical properties of the V0 and V1 alloys at different fluences. The average hardness

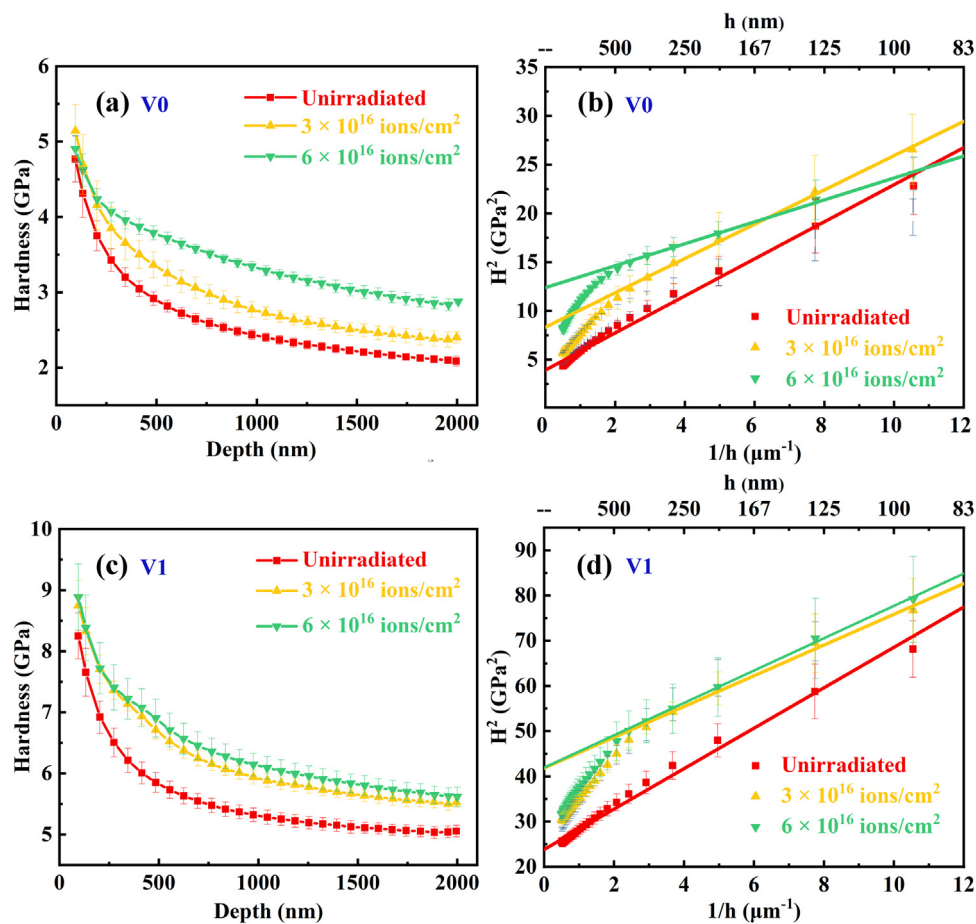


Fig. 9. Results of the nanoindentation test of the V0 and V1 alloys: (a and c) average hardness measurements as a function of depth of the pristine and irradiated samples; (b and d) corresponding profiles of H^2 versus $1/h$.

plotted as a function of depth for the pristine and irradiated samples of V0 and V1 alloys is shown in Fig. 9a and 9c, respectively. As observed from the curves of the two alloys, the hardness values of the irradiated samples were significantly higher than those of the pristine samples at the same depth, indicating that He-ion implantation led to the hardening of the two alloys.

Based on the model relating to the indentation size effect proposed by Nix and Gao [42,61], the nanoindentation measurements of the V0 and V1 alloys were plotted as H^2 versus $1/h$ (where h is the depth from the surface and H is the corresponding measured hardness), which are exhibited in Fig. 9b and 9d, respectively. Considering the surface effect and softer substrate effect [42], the hardness values measured in the depth range of 80–350 nm were selected for fitting to obtain the irradiation-induced hardness at a certain level. Within the selected depth range, the H^2 versus $1/h$ showed a good linear fitting for the pristine and irradiated samples of the two alloys. The values of the hardness, hardness increment (hardness difference between the pristine and irradiated samples), and hardening fraction (ratio of hardness increment to the hardness of pristine sample) of the V0 and V1 alloys obtained by fitting are summarized in Table 5. At fluences of 3×10^{16} and 6×10^{16} ions/cm², the hardness increments of the samples were 0.98, 1.53 GPa for the V0 alloy and 1.59, 1.59 GPa for the V1 alloy. The irradiation fluence dependence of hardness, hardness increment, and hardening fraction of the two alloys are shown in Fig. 10a–10c, respectively. Obviously, with increasing displacement damage, the irradiation-induced hardening gradually enhanced in the V0 alloy. However, the hardness increment of the V1 alloy remained almost unchanged at the two fluences, which was simi-

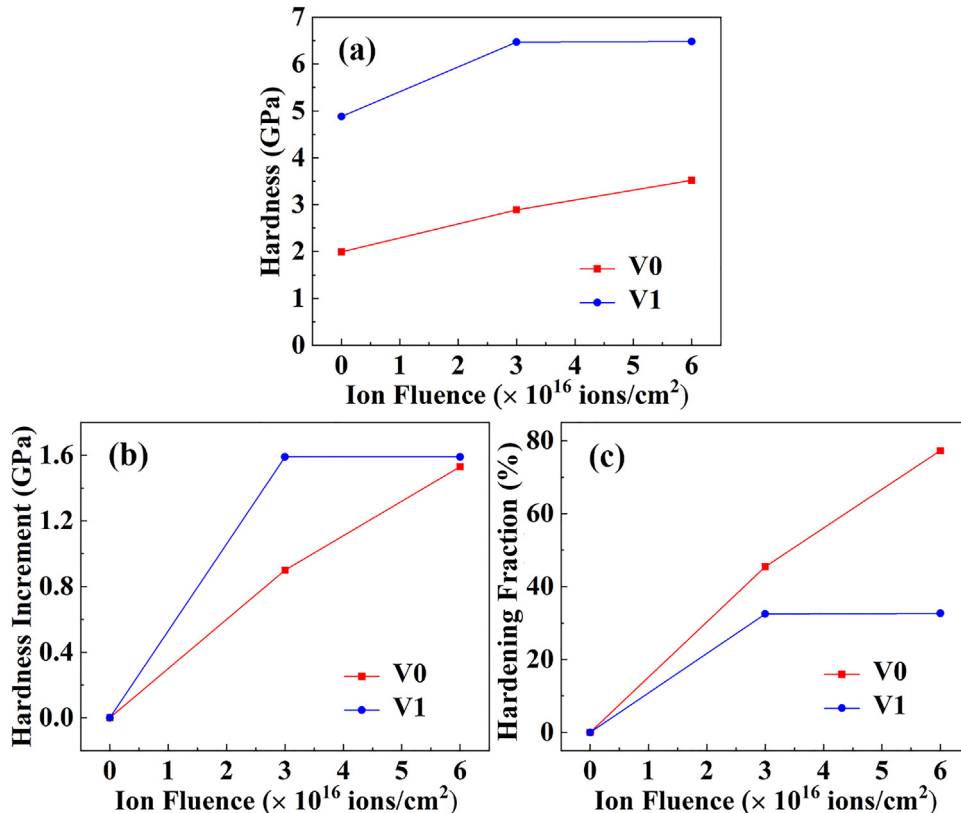
lar to the irradiation-induced hardening saturation results of traditional alloys [62–64]. At each fluence, the hardening fraction of the V1 alloy was lower than that of the V0 alloy, indicating that the V1 alloy had a better irradiation-induced hardening resistance.

The irradiation-induced hardening and embrittlement could degrade the mechanical properties of the materials under extreme conditions, thereby threatening the safety and stability of reactor operation. The V0 alloy with the FCC structure showed a higher hardening fraction. An irradiation-induced hardening saturation was observed in the V1 alloy, which meant that under the specified irradiation condition, the change in size and number density of the defects could no longer improve the hardness. Additionally, the low hardening fraction of the V1 alloy (33%) reflected that the irradiation-induced hardening resistance of the novel low-activation HEA was superior to that of most conventional materials [8,57–59]. The outstanding irradiation performance might be attributed to the low residual defect density caused by the enhanced point defect recombination in the BCC-structured V1 alloy. In recent studies, HEAs with BCC structure, such as Ti₂ZrHfV_{0.5}Mo_{0.2} [1], HfNbTaTiZr [34], and W₃₈Ta₃₆Cr₁₅V₁₁ [27] alloys, have also shown excellent irradiation-induced hardening resistance with low hardening fraction, which could be related to the efficient self-healing and recombination process of the defects produced by irradiation. Based on the ab initio calculations, Zhao [25] proposed that a larger overlap region was exhibited in the migration energy spectrum of vacancies and interstitials in BCC-structured HEAs, favoring the defect recombination. Thus, the hindrance to dislocation movement could be weakened due to the suppressed residual defect density in the V1 alloy, and the irradiation-induced hardening

Table 5

Nanoindentation test results of the V0 and V1 alloys.

Alloy	Fluence (ions/cm ²)	Hardness (GPa)	Hardness increment (GPa)	Hardening fraction (%)
V0	0	1.99	0	0
	3×10^{16}	2.97	0.98	45
	6×10^{16}	3.52	1.53	77
V1	0	4.88	0	0
	3×10^{16}	6.47	1.59	33
	6×10^{16}	6.47	1.59	33

**Fig. 10.** Line charts of nanoindentation test results for the V0 and V1 alloys: (a) hardness, (b) hardness increment, and (c) hardening fraction.

resistance was improved. Further investigation is needed to explore the effects of structure on the irradiation-induced hardening resistance of HEAs. In addition, the compositions play an important role in irradiation performance of the alloys. The irradiation results showed that, compared with the V-free alloy, the addition of V element with the largest atomic radius of the five selected elements possessed an affirmative effect on improving irradiation-induced hardening resistance of the V1 alloy. This was similar to the findings in traditional materials, that is, the elements with the larger atomic radius could improve the irradiation resistance of the alloys [63,65]. Moreover, the impact of the morphology and the number density of He bubble on hardening should not be ignored for the He-ion implanted alloys [64,66]. The high internal pressure in the He bubbles could provide enhanced respective barrier strengths, contributing to alloy hardening. The internal pressure of spherical He bubbles decreased with the increase in size, and the cracks or deformation-induced curvature change of the He bubbles could further reduce the internal pressure, weakening the effect on hardening. And the interaction between the He bubble and dislocation could be suppressed for the lower number density of He bubbles in V1 alloy. Considering the larger and faceted bubbles with lower number density, the V1 alloy showed a better irradiation performance than the V0 alloy.

4. Conclusions

In this study, the Co-free $V_xCrFeMnNi_y$ ($x = 0, y = 2; x = 1, y = 0$; the alloys were denoted as V0 and V1, respectively) HEAs were designed and prepared. The microstructures, mechanical properties, and irradiation tolerance of the alloys were investigated, and the main results were as follows:

- (1) The structure of the $V_xCrFeMnNi_y$ alloys changed from a single-phase FCC solid solution structure for the V0 alloy to a single-phase BCC structure for the V1 alloy with the addition of V element. The V1 alloy possessed fine comprehensive mechanical properties with a yield strength of 660 MPa.
- (2) At fluences of 3×10^{16} and 6×10^{16} ions/cm², no phase transformation or precipitation could be found in the V0 and V1 alloys at 1023 K. The He bubble peak regions (at the depth of ~1600 to 1900 nm) of the two alloys remained almost unchanged at different fluences, and the He bubbles showed a uniform and random spatial distribution. Spherical He bubbles were detected in the V0 alloy at both fluences, while the shape of the He bubbles in the V1 alloy changed from faceted to spherical as the fluence increased.
- (3) The average size of the He bubbles increased from 2.3 ± 0.6 to 3.4 ± 1.0 nm for the V0 alloy, and from 2.8 ± 0.9 to

- 3.6 ± 1.1 nm for the V1 alloy with the increase in fluence. At each fluence, the average size of the He bubbles in the V1 alloy was slightly larger than that in the V0 alloy, while the number density and volume fraction were lower.
- (4) The FCC-structured V0 alloy exhibited a higher hardening fraction, and an irradiation-induced hardening saturation was observed in the BCC-structured V1 alloy, with a low hardening fraction of 33%. The outstanding irradiation performance of the V1 alloy might be attributed to the lower number density of He bubbles, suppressed residual defect density, and good structural stability.

Declaration of Competing Interest

The authors declare that they have no known competing financial interests or personal relationships that could have appeared to influence the work reported in this paper.

CRediT authorship contribution statement

Huanzhi Zhang: Conceptualization, Data curation, Formal analysis, Investigation, Writing – original draft, Writing – review & editing. **Chunhui Li:** Conceptualization, Data curation, Formal analysis, Investigation, Writing – original draft, Writing – review & editing. **Zhenbo Zhu:** Data curation, Software. **Hefei Huang:** Data curation, Software. **Tongmin Wang:** Writing – review & editing. **Tinigju Li:** Formal analysis, Investigation, Supervision, Funding acquisition, Writing – review & editing, Project administration.

Data Availability

No data was used for the research described in the article.

Acknowledgments

Supported by the National Key Research and Development Program of China (No. 2019YFA0209901), Liao Ning Revitalization Talents Program (No. XLYC1807047) and Major Special Project of “Scientific and Technological Innovation 2025” in Ningbo (No. 2019B10086).

References

- [1] Y. Lu, H. Huang, X. Gao, C. Ren, J. Gao, H. Zhang, S. Zheng, Q. Jin, Y. Zhao, C. Lu, T. Wang, T. Li, A promising new class of irradiation tolerant materials: $\text{ti}_2\text{ZrHfV}_{0.5}\text{Mo}_{0.2}$ high-entropy alloy, *J. Mater. Sci. Technol.* 35 (2019) 369–373.
- [2] T. Shi, Z. Su, J. Li, C. Liu, J. Yang, X. He, D. Yun, Q. Peng, C. Lu, Distinct point defect behaviours in body-centered cubic medium-entropy alloy NbZrTi induced by severe lattice distortion, *Acta Mater.* 229 (2022) 117806.
- [3] Q. Xu, T. Zhu, Z.H. Zhong, X.Z. Cao, H. Tsuchida, Investigation of irradiation resistance characteristics of precipitation strengthened high-entropy alloy ($\text{CoCrFeNi})_{95}\text{Ti}_1\text{Nb}_1\text{Al}_3$ using slow positron beam, *J. Alloy. Compd.* 888 (2021) 161518.
- [4] K. Jin, C. Lu, L.M. Wang, J. Qu, W.J. Weber, Y. Zhang, H. Bei, Effects of compositional complexity on the ion-irradiation induced swelling and hardening in Ni-containing equiatomic alloys, *Scr. Mater.* 119 (2016) 65–70.
- [5] C. Lu, L. Niu, N. Chen, K. Jin, T. Yang, P. Xiu, Y. Zhang, F. Gao, H. Bei, S. Shi, M.R. He, I.M. Robertson, W.J. Weber, L. Wang, Enhancing radiation tolerance by controlling defect mobility and migration pathways in multicomponent single-phase alloys, *Nat. Commun.* 7 (2016) 13564.
- [6] P.P. Liu, M.Z. Zhao, Y.M. Zhu, J.W. Bai, F.R. Wan, Q. Zhan, Effects of carbide precipitate on the mechanical properties and irradiation behavior of the low activation martensitic steel, *J. Alloy. Compd.* 579 (2013) 599–605.
- [7] Q. Yuan, A. Chauhan, E. Gaganidze, J. Aktaa, *In-situ* TEM investigations of dislocation loop annealing kinetics in neutron-irradiated 9%Cr RAFM steel, *J. Nucl. Mater.* 558 (2022) 153365.
- [8] Z.F. Wu, L.D. Xu, H.Q. Chen, Y.X. Liang, J.L. Du, Y.F. Wang, S.L. Zhang, X.C. Cai, B.R. Sun, J. Zhang, T.D. Shen, J. Wang, E.G. Fu, Significant suppression of void swelling and irradiation hardening in a nanograined/nanoprecipitated 14YWT-ODS steel, *J. Nucl. Mater.* 559 (2022) 153480.
- [9] C. Doñate-Buendía, P. Kürnsteiner, F. Stern, M.B. Wilms, R. Streubel, I.M. Kusoglu, J. Tenkamp, E. Bruder, N. Pirch, S. Barcikowski, K. Durst, J.H. Schleifbaum, F. Walther, B. Gault, B. Gökce, Microstructure formation and mechanical properties of ODS steels built by laser additive manufacturing of nanoparticle coated iron-chromium powders, *Acta Mater.* 206 (2021) 116566.
- [10] H. Luo, F. Luo, Y. Chen, J. Wang, Q. Liu, F. Li, Z. Xie, W. Lin, L. Guo, Effect of yttrium content on microstructure and irradiation behavior of V-4Cr-4Ti-xY alloys, *J. Nucl. Mater.* 559 (2022) 153480.
- [11] Z.Q. Wang, Q. Zhao, Y.P. Wei, P.P. Liu, S.W. Yang, F.R. Wan, Q. Zhan, The direct correlation between precipitate-size-dependent strain at the interface and the irradiation hardening in V-4Cr-4Ti, *J. Alloy. Compd.* 732 (2018) 406–413.
- [12] S.J. Zinkle, A. Möslang, Evaluation of irradiation facility options for fusion materials research and development, *Fusion Eng. Des.* 88 (2013) 472–482.
- [13] S. Agarwal, G. Duschler, Y. Zhao, M.L. Crespiolo, Y. Katoh, W.J. Weber, Multiscale characterization of irradiation behaviour of ion-irradiated SiC/Si composites, *Acta Mater.* 161 (2018) 207–220.
- [14] J.W. Yeh, S.K. Chen, S.J. Lin, J.Y. Gan, T.S. Chin, T.T. Shun, C.H. Tsau, S.Y. Chang, Nanostructured high-entropy alloys with multiple principal elements: novel alloy design concepts and outcomes, *Adv. Eng. Mater.* 6 (2004) 299–303.
- [15] B. Cantor, I.T.H. Chang, P. Knight, A.J.B. Vincent, Microstructural development in equiatomic multicomponent alloys, *Mater. Sci. Eng. A Struct. Mater. Prop. Microstruct. Process.* 375–377 (2004) 213–218.
- [16] M.C. Gao, J.W. Yeh, P.K. Liaw, Y. Zhang, *High-Entropy Alloys: Fundamentals and Applications*, Springer Nature Publishing, Switzerland, 2016.
- [17] B. Schuh, F. Mendez-Martin, B. Völker, E.P. George, H. Clemens, R. Pippan, A. Hohenwarter, Mechanical properties, microstructure and thermal stability of a nanocrystalline CoCrFeMnNi high-entropy alloy after severe plastic deformation, *Acta Mater.* 96 (2015) 258–268.
- [18] M. Behera, A. Panigrahi, M. Bönisch, G. Shankar, P.K. Mishra, Structural stability and thermal expansion of TiTaNbMoZr refractory high entropy alloy, *J. Alloy. Compd.* 892 (2022) 162154.
- [19] O.N. Senkov, J.K. Jensen, A.L. Pilchak, D.B. Miracle, H.L. Fraser, Compositional variation effects on the microstructure and properties of a refractory high-entropy superalloy $\text{AlMo}_{0.5}\text{NbTa}_{0.5}\text{TiZr}$, *Mater. Des.* 139 (2018) 498–511.
- [20] S. Wu, D. Qiao, H. Zhao, J. Wang, Y. Lu, A novel $\text{NbTaW}_{0.5}(\text{Mo}_2\text{C})_x$ refractory high-entropy alloy with excellent mechanical properties, *J. Alloy. Compd.* 889 (2021) 161800.
- [21] C. Shang, E. Axinte, J. Sun, X. Li, P. Li, J. Du, P. Qiao, Y. Wang, $\text{CoCrFeNi}(\text{W}_{1-x}\text{Mo}_x)$ high-entropy alloy coatings with excellent mechanical properties and corrosion resistance prepared by mechanical alloying and hot pressing sintering, *Mater. Des.* 117 (2017) 193–202.
- [22] J.J. Zhang, X.L. Yin, Y. Dong, Y.P. Lu, L. Jiang, T.M. Wang, T.J. Li, Corrosion properties of $\text{Al}_x\text{CoCrFeNiTi}_{0.5}$ high entropy alloys in 0.5M H_2SO_4 aqueous solution, *Mater. Res. Innov.* 18 (2014) S4–756–S754–760.
- [23] Y. Zhang, J.W. Yeh, J.F. Sun, J.P. Lin, Y. Ke-Fu, High-entropy alloys, *Adv. Mater. Sci. Eng.* 2015 (2015) 1–1.
- [24] C. Lu, K. Jin, L.K. Béland, F. Zhang, T. Yang, L. Qiao, Y. Zhang, H. Bei, H.M. Christen, R.E. Stoller, Direct observation of defect range and evolution in ion-irradiated single crystalline Ni and Ni binary alloys, *Sci. Rep.* 6 (2016) 19994.
- [25] S. Zhao, Defect properties in a VTaCrW equiatomic high entropy alloy (HEA) with the body centered cubic (bcc) structure, *J. Mater. Sci. Technol.* 44 (2020) 133–139.
- [26] O. El-Atwani, N. Li, M. Li, A. Devaraj, E.J.E.A. Martinez, Outstanding radiation resistance of tungsten-based high entropy alloys, *Sci. Adv.* 5 (3) (2019) eaav2002.
- [27] Z. Zhang, E.H. Han, C. Xiang, Irradiation behaviors of two novel single-phase bcc-structure high-entropy alloys for accident-tolerant fuel cladding, *J. Mater. Sci. Technol.* 84 (2021) 230–238.
- [28] M.R. He, S. Wang, K. Jin, H. Bei, K. Yasuda, S. Matsumura, K. Higashida, I.M. Robertson, Enhanced damage resistance and novel defect structure of Cr-FeCoNi under *in situ* electron irradiation, *Scr. Mater.* 125 (2016) 5–9.
- [29] L. Koch, F. Granberg, T. Brink, D. Utt, K. Albe, F.G. Djurabekova, K.J. Nordlund, Local segregation versus irradiation effects in high-entropy alloys: steady-state conditions in a driven system, *J. Appl. Phys.* 122 (2017) 105106.
- [30] S.Q. Xia, Z. Wang, T.F. Yang, Y. Zhang, Irradiation behavior in high entropy alloys, *J. Iron Steel Res. Int.* 22 (2015) 879–884.
- [31] C. Lu, T. Yang, K. Jin, N. Gao, P. Xiu, Y. Zhang, F. Gao, H. Bei, W.J. Weber, K. Sun, Y. Dong, L. Wang, Radiation-induced segregation on defect clusters in single-phase concentrated solid-solution alloys, *Acta Mater.* 127 (2017) 98–107.
- [32] M.R. He, S. Wang, S. Shi, K. Jin, H. Bei, K. Yasuda, S. Matsumura, K. Higashida, I.M. Robertson, Mechanisms of radiation-induced segregation in Cr-FeCoNi-based single-phase concentrated solid solution alloys, *Acta Mater.* 126 (2017) 182–193.
- [33] Y. Zhang, G.M. Stocks, K. Jin, C. Lu, H. Bei, B.C. Sales, L. Wang, L.K. Béland, R.E. Stoller, G.D. Samolyuk, M. Caro, A. Caro, W.J. Weber, Influence of chemical disorder on energy dissipation and defect evolution in concentrated solid solution alloys, *Nat. Commun.* 6 (2015) 8736.
- [34] A. Kareer, J.C. Waite, B. Li, A. Couet, D.E.J. Armstrong, A.J. Wilkinson, Short communication: low activation, refractory, high entropy alloys for nuclear applications, *J. Nucl. Mater.* 526 (2019) 151744.
- [35] C. Li, X. Hu, T. Yang, N.K. Kumar, S.J. Zinkle, Neutron irradiation response of a Co-free high entropy alloy, *J. Nucl. Mater.* 527 (2019) 151838.
- [36] A. Ayyagari, R. Salloom, S. Muskeri, S. Mukherjee, Low activation high entropy alloys for next generation nuclear applications, *Materialia* 4 (2018) 99–103.
- [37] M. Sadeghilaridjani, A. Ayyagari, S. Muskeri, V. Hasannaeimi, R. Salloom, W.Y. Chen, S. Mukherjee, Ion irradiation response and mechanical behavior of reduced activity high entropy alloy, *J. Nucl. Mater.* 529 (2020) 151955.
- [38] W. Zhang, P.K. Liaw, Y. Zhang, A novel low-activation $\text{VCrFeTa}_x\text{W}_x$ ($x = 0.1, 0.2, 0.3, 0.4$, and 1) high-entropy alloys with excellent heat-softening resistance, *Entropy* 20 (12) (2018) 951.
- [39] Z. Sun, X. Li, Z. Wang, Microstructure and mechanical properties of low acti-

- vation Fe-Ti-Cr-V-W multi-principal element alloys, *J. Nucl. Mater.* 533 (2020) 152078.
- [40] R.L. Klueh, A.T. Nelson, Ferritic/martensitic steels for next-generation reactors, *J. Nucl. Mater.* 371 (2007) 37–52.
- [41] D. Chen, S. Zhao, J. Sun, P. Tai, Y. Sheng, Y. Zhao, G. Yeli, W. Lin, S. Liu, W. Kai, J.J. Kai, Diffusion controlled helium bubble formation resistance of FeCoNiCr high-entropy alloy in the half-melting temperature regime, *J. Nucl. Mater.* 526 (2019) 151747.
- [42] Z. Zhu, H. Huang, O. Muránsky, J. Liu, Z. Zhu, Y. Huang, On the irradiation tolerance of nano-grained Ni-Mo-Cr alloy: 1 MeV He⁺ irradiation experiment, *J. Nucl. Mater.* 544 (2021) 152694.
- [43] M. Cui, J. Wang, Z. Wang, T. Shen, K. Wei, C. Yao, J. Sun, N. Gao, Y. Zhu, L. Pang, D. Wang, H. Zhu, Y. Han, X. Fang, Helium irradiation induced hardening in MNHS steels, *Nucl. Instrum. Mater. B* 406 (2017) 611–617.
- [44] S. Guo, C. Ng, J. Lu, C.T. Liu, Effect of valence electron concentration on stability of fcc or bcc phase in high entropy alloys, *J. Appl. Phys.* 109 (10) (2011) 103505.
- [45] Y. Zhang, Y.J. Zhou, J.P. Lin, G.L. Chen, P.K. Liaw, Solid-Solution phase formation rules for multi-component alloys, *Adv. Eng. Mater.* 10 (2008) 534–538.
- [46] X. Yang, Y. Zhang, Prediction of high-entropy stabilized solid-solution in multi-component alloys, *Mater. Chem. Phys.* 132 (2012) 233–238.
- [47] F. Hofmann, D. Nguyen-Manh, M.R. Gilbert, C.E. Beck, J.K. Eliason, A.A. Maznev, W. Liu, D.E. Armstrong, K.A. Nelson, S.L. Dudarev, Lattice swelling and modulus change in a helium-implanted tungsten alloy: x-ray micro-diffraction, surface acoustic wave measurements, and multiscale modelling, *Acta Mater.* 89 (2015) 352–363.
- [48] C.A. Taylor, M.K. Patel, J.A. Aguiar, Y. Zhang, M.L. Crespiello, J. Wen, H. Xue, Y. Wang, W.J. Weber, Bubble formation and lattice parameter changes resulting from He irradiation of defect-fluorite Gd₂Zr₂O₇, *Acta Mater.* 115 (2016) 115–122.
- [49] Y. Zhang, M.A. Tunes, M.L. Crespiello, F. Zhang, W.L. Boldman, P.D. Rack, L. Jiang, C. Xu, G. Greaves, S.E. Donnelly, L. Wang, W.J. Weber, Thermal stability and irradiation response of nanocrystalline CoCrCuFeNi high-entropy alloy, *Nanotechnology* 30 (2019) 294004.
- [50] F. Wang, X. Yan, T. Wang, Y. Wu, L. Shao, M. Nastasi, Y. Lu, B. Cui, Irradiation damage in (Zr_{0.25}Ta_{0.25}Nb_{0.25}Tl_{0.25})C high-entropy carbide ceramics, *Acta Mater.* 195 (2020) 739–749.
- [51] N. Jia, Y. Li, H. Huang, S. Chen, D. Li, Y. Dou, X. He, W. Yang, Y. Xue, K. Jin, Helium bubble formation in refractory single-phase concentrated solid solution alloys under MeV He ion irradiation, *J. Nucl. Mater.* 550 (2021) 152937.
- [52] A. Ofan, L. Zhang, O. Gaathon, S. Bakhrus, H. Bakhrus, Y. Zhu, D. Welch, R.M. Osgood, Spherical solid He nanometer bubbles in an anisotropic complex oxide, *Phys. Rev. B* 82 (2010) 104113.
- [53] F. Granberg, X. Wang, D. Chen, K. Jin, Y. Wang, H. Bei, W.J. Weber, Y. Zhang, K.L. More, K. Nordlund, F. Djurabekova, Origin of increased helium density inside bubbles in Ni_(1-x)Fe_x alloys, *Scr. Mater.* 191 (2021) 1–6.
- [54] X.L. Zhou, H.F. Huang, R. Xie, G.J. Thorogood, C. Yang, Z.J. Li, H.J. Xu, Helium ion irradiation behavior of Ni-1wt.%SiC_{NP} composite and the effect of ion flux, *J. Nucl. Mater.* 467 (2015) 848–854.
- [55] J. Bai, J. Li, C. Fu, C. Ren, S. Chen, Y. Li, Z. Li, Q. Chen, Z. Zhu, J. Lin, Effect of helium bubbles on the irradiation hardening of GH3535 welded joints at 650°C, *J. Nucl. Mater.* 557 (2021) 153241.
- [56] C. Fu, J. Li, J. Bai, Y. Li, Q. Chen, G. Lei, J. Lin, Z. Zhu, Y. Meng, Effect of helium bubbles on irradiation hardening of additive manufacturing 316L stainless steel under high temperature He ions irradiation, *J. Nucl. Mater.* 550 (2021) 152948.
- [57] S. Jiang, C. Yu, P. Zheng, L. Guo, X. Zhou, W.F. Rao, Bubbles and precipitates formation and effects on the hardening of irradiated vanadium alloys, *J. Nucl. Mater.* 544 (2021) 152712.
- [58] P.P. Liu, W.T. Han, X.O. Yi, Q. Zhan, F.R. Wan, Effect of He and H synergy on mechanical property of ion-irradiated Fe-10Cr alloy, *Fusion Eng. Des.* 129 (2018) 221–229.
- [59] Z.Y. Fu, P.P. Liu, F.R. Wan, Q. Zhan, Helium and hydrogen irradiation induced hardening in CLAM steel, *Fusion Eng. Des.* 91 (2015) 73–78.
- [60] S. Liu, W. Lin, D. Chen, B. Han, S. Zhao, F. He, H. Niu, J.J. Kai, Effects of temperature on helium cavity evolution in single-phase concentrated solid-solution alloys, *J. Nucl. Mater.* 557 (2021) 153261.
- [61] W.C. Oliver, G.M. Pharr, An improved technique for determining hardness and elastic modulus using load and displacement sensing indentation experiments, *J. Mater. Res.* 7 (2011) 1564–1583.
- [62] T. Miyazawa, T. Nagasaka, R. Kasada, Y. Hishinuma, T. Muroga, H. Watanabe, T. Yamamoto, S. Nogami, M. Hatakeyama, Evaluation of irradiation hardening of ion-irradiated V-4Cr-4Ti and V-4Cr-4Ti-0.15Y alloys by nanoindentation techniques, *J. Nucl. Mater.* 455 (2014) 440–444.
- [63] Y. Yang, C. Zhang, Y. Meng, J. Liu, J. Gou, Y. Xian, Y. Song, Nanoindentation on V-4Ti alloy irradiated by H and He ions, *J. Nucl. Mater.* 459 (2015) 1–4.
- [64] Y. Yang, S.H. Kang, C. Zhang, J. Jang, Nanoindentation on an oxide dispersion strengthened steel and a ferritic/martensitic steel implanted with He ions, *J. Nucl. Mater.* 455 (2014) 325–329.
- [65] Y. Candra, K. Fukumoto, A. Kimura, H.J. Matsui, Microstructural evolution and hardening of neutron irradiated vanadium alloys at low temperatures in Japan material testing reactor, *J. Nucl. Mater.* 271–272 (1999) 301–305.
- [66] H. Trinkaus, B.N. Singh, Helium accumulation in metals during irradiation – where do we stand? *J. Nucl. Mater.* 323 (2003) 229–242.